Applied Physics A (2018) 124:675
https://doi.org/10.1007/s00339-018-2092-5

Applied Physics A
Materials Science & Processing

Influence of temperature on structure, morphology, and magnetic property of graphene–$MnFe_2O_4$ nanocomposites synthesized by a combined hydrothermal/co-precipitation method

Tran V. Thu[1,2] · **Vu D. Thao**[2]

Received: 24 June 2018 / Accepted: 2 September 2018 / Published online: 10 September 2018

Abstract
Combination of co-precipitation and hydrothermal methods is a promising route to synthesize various materials. Herein, we synthesized reduced graphene oxide/manganese ferrite (rGO/$MnFe_2O_4$) nanocomposites through combining a co-precipitation reaction of Mn^{2+} and Fe^{3+} ions in GO solution with subsequent hydrothermal treatment at different temperatures (80, 130, and 180 °C). The resulting rGO/$MnFe_2O_4$ nanocomposites were characterized using X-ray diffractometry, Fourier-transform infrared spectroscopy, scanning and transmission electron microscopy, and magnetic measurements at room temperature. The influence of hydrothermal temperature on structural, morphological, magnetic and As(III) adsorption properties of rGO/$MnFe_2O_4$ nanocomposites was studied. Increasing hydrothermal temperature leads to better crystallinity, magnetic properties, and As(III) adsorption capacity. At the hydrothermal temperature of 180 °C, the resulting rGO/$MnFe_2O_4$ nanocomposites exhibited a crystalline size of 37.2 nm, saturated magnetization of 22.7 emu/g, and As(III) removal efficiency of 83% at neutral pH (pH ≈ 7).

1 Introduction

In recent years, reduced graphene oxide/manganese ferrite (rGO/$MnFe_2O_4$) nanocomposites have been attracting numerous research interests due to their potential applications such as microwave absorption [1], high-density energy storage [2], sensing [3], antibacterial [4], lithium storage [5–7], advanced hyperthermia and magnetic biomarker in biosensing [8], magnetic resonance imaging, photothermal therapy and drug delivery [9], and supercapacitor [2, 10]. rGO/$MnFe_2O_4$ nanocomposites could be also used as adsorbent or catalyst thanks to their high specific surface area, high stability towards oxidation, and large saturated magnetization [11–15]. Notably, rGO/$MnFe_2O_4$ nanocomposites exhibit a high adsorption capacity towards various pollutants such as glyphosate [16], As(V) [17], and particularly As(III), one of the most toxic contaminants in aqueous environment [11]. It has been widely realized that various properties of $MnFe_2O_4$-based materials are strongly correlated with their physical dimensions and morphology [18]. Therefore, the development of novel routes for the synthesis of such materials and understanding the synthesis−structure−property relationship play critical roles in the progress of the field.

rGO/$MnFe_2O_4$ nanocomposites have been synthesized by a wide range of methods such as co-precipitation [5, 6, 8, 11, 17], hydrothermal [1, 2, 7], and thermal decomposition [9]. It has been known that co-precipitation and hydrothermal routes are among the most common methods for the preparation of crystalline materials, particularly metal oxides [12]. Co-precipitation method has been widely adopted because of its advantages including simplicity and the unnecessity of high-temperature equipments. However, the obtained materials have low crystallinity and saturated magnetization [11, 19, 20], causing the separation and recycling of these materials inconvenient. To improve magnetic properties, the materials obtained from co-precipitation reaction are often subjected to an annealing step. Nevertheless, high-temperature annealing unavoidably causes aggregation, therefore, post-annealing materials have reduced surface area and limited dispersibility. On the other side, hydrothermal method is considered a promising route for the synthesis of various crystalline materials at relatively low temperature

✉ Tran V. Thu
thutv@mta.edu.vn

[1] Institute of Research and Development, Duy Tan University, K7/25 Quang Trung, Danang 550000, Vietnam

[2] Department of Chemical Engineering, Le Quy Don Technical University, 236 Hoang Quoc Viet, Hanoi 100000, Vietnam

(< 200 °C). In hydrothermal synthesis, the crystallization of desired materials is affected by many factors, including the type and concentration of precursors, solvent, and/or morphology-controlling agents. Therefore, a careful control over chemical compositions of hydrothermal mixture is required for ease of control over crystallinity and morphology. Based on these considerations, a combined hydrothermal/co-precipitation route might offer many advantages compared to that of individual ones. As far as the authors are aware, the combination of co-precipitation and hydrothermal methods for the synthesis of rGO/$MnFe_2O_4$ nanocomposites has not been reported. Moreover, the influence of hydrothermal temperature on the structure, morphology, and magnetic properties of the resulting nanocomposites was not investigated. Additionally, little work has been carried out to use rGO/$MnFe_2O_4$ for As(III) adsorption.

In this work, we describe the combination of co-precipitation and hydrothermal methods for the synthesis of rGO/$MnFe_2O_4$ nanocomposites. The nanocomposites are formed by co-precipitation of Mn^{2+} and Fe^{3+} ions in an alkaline environment containing GO, followed by hydrothermal treatment at different temperatures. The structural, morphological, magnetic, and As(III) adsorption properties of the resulting rGO/$MnFe_2O_4$ nanocomposites were thoroughly investigated to understand the influence of hydrothermal temperature. The method described here is simple, facile, and can be extended to a wider range of metal ferrites MFe_2O_4 (M = Co/Ni/Cu/Zn).

2 Materials and methods

2.1 Materials

Sodium hydroxide (NaOH), ethanol (C_2H_5OH 99.5%), iron(III) chloride hexahydrate ($FeCl_3{\cdot}6H_2O$, 99%) and manganese chloride tetrahydrate ($MnCl_2{\cdot}4H_2O$) were purchased from Shanghai Aladdin Bio-Chem Technology Co., Ltd. All the reagents were of analytical grade and used without further purification.

2.2 Synthesis of rGO/$MnFe_2O_4$ nanocomposites

GO was synthesized according to our previously published works [21–23]. rGO/$MnFe_2O_4$ nanocomposites were synthesized using GO, Mn^{2+}, and Fe^{3+} salts as precursors (Fig. 1). GO (0.45 g), Mn^{2+} (0.01 mol), and Fe^{3+} (0.02 mol) were dissolved in 300 ml DI water and mechanically stirred for 2 h. A 2 M NaOH solution was slowly dropped into the above solution until pH ≈ 11 (It is advised that the reversion of this addition sequence might result in materials with different properties [24, 25]). The co-precipitation reaction was maintained for 4 h under mechanical stirring at room temperature.

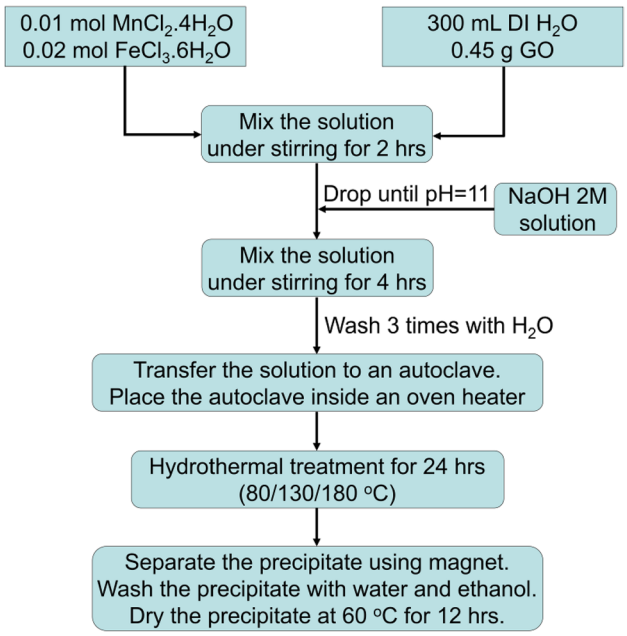

Fig. 1 Synthesis flowchart of rGO/$MnFe_2O_4$ nanocomposites by combined hydrothermal/co-precipitation route

The as-obtained slurry was washed with DI water, transferred to a Teflon-lined autoclave and placed inside a conventional heater. The hydrothermal treatment was performed at designated temperatures (80, 130, and 180 °C) for 24 h. The obtained precipitate was separated from the reaction mixture using a permanent magnet, washed several times with DI water and ethanol, and dried at 60 °C for 12 h. The as-synthesized rGO/$MnFe_2O_4$ was received in the blackish-brown, powdery form.

2.3 Characterization

X-ray diffractometry (XRD) analysis was performed on a Siemens D5000 X-ray diffractometer (30 kV/40 mA; $\lambda = 1.5406$ Å). Crystallite size of $MnFe_2O_4$ was calculated using Scherrer equation [26]:

$$d = k \cdot \lambda / (\beta \cdot \cos\theta) \quad (1)$$

where λ is the wavelength of Cu Kα irradiation, $\lambda = 1.5406$ Å, β is the full width at maximal half (FWHM), θ is Bragg diffraction angle (peak position), $k = 0.9$. Fourier-transform infrared (FTIR) spectra were collected on a Perkin-Elmer Spectrum Two spectrometer equipped with a universal attenuated total reflectance (UATR) accessory. Raman spectra were acquired on a Horiba Scientific T64000 Raman spectrometer. The thermal stability of the synthesized materials was studied by thermogravimetric analysis (Pyris 1 TGA, Perkin–Elmer). Scanning electron microscopy (SEM) images and energy-dispersive X-ray (EDX) spectra

were collected on a Jeol JSM-6510LV scanning electron microscope equipped with an energy-dispersive X-ray analyzer. Transmission electron microscopy (TEM) images were observed using a Jeol JEM-1010 transmission electron microscope. The magnetization curves were collected on a custom-built vibrating sample magnetometer.

2.4 As(III) adsorption study

$rGO/MnFe_2O_4$ nanocomposites synthesized at different temperatures were used as adsorbent.

Batch adsorption experiments were carried out in 250-mL conical flasks containing 40 mL of As(III) solution (100 µg/l) each. 0.01 g $rGO/MnFe_2O_4$ nanocomposites were added to each of the above flask and mechanically stirred at 25 °C. Adsorption experiments were performed at different pH values (4, 7, 10), maintained by adding either 0.1 M HCl or 0.1 M NaOH solutions. To avoid the possible oxidation of As(III), all adsorption experiments were conducted in the dark. After an equilibrium time of 2 h, the solutions were centrifuged and a magnet was used to collect $rGO/MnFe_2O_4$ nanocomposites. The remaining concentration of As(III) was analyzed using inductively coupled plasma-optical emission spectrometry (ICP-OES). The As(III) removal efficiency (H, %) was calculated using the following equation:

$$H = (C_0 - C_e) \times 100/C_0 \quad (2)$$

where C_0 and C_e are the initial and equilibrium concentrations of As(III), correspondingly.

3 Results and discussion

Figure 2 shows XRD patterns of $rGO/MnFe_2O_4$ nanocomposites synthesized at different hydrothermal temperatures. In the XRD patterns of $rGO/MnFe_2O_4$ synthesized at 180 °C, all prominent peaks at 30.35° (2.94 Å), 35.65° (2.52 Å), 43.35° (2.09 Å), 53.55° (1.71 Å), 57.25° (1.61 Å), and 62.65° (1.48 Å) can be well indexed to (220), (311), (400), (422), (511), and (440) lattice planes of face-centered cubic structure of spinel-type, jacobsite manganese ferrite (JCPDS no. 10-0319) [20]. The peak at 32.05° (2.79 Å) is possibly due to (104) lattice plane of α-Fe_2O_3 crystalline phase [27]. Given the fact that metallic ions have been mixed in proper stoichiometry (Mn^{2+}:Fe^{3+} = 1:2 in molar ratio), it is thought that the $rGO/MnFe_2O_4$ nanocomposites consist of an Mn-deficient layer on the outer surface. Whereas the typical diffraction peaks of rGO are not clearly observed, indicating that the re-stacking of rGO sheets is efficiently inhibited by the presence of $MnFe_2O_4$ nanocrystals at high density on their planar surface. For $rGO/MnFe_2O_4$ nanocomposite samples synthesized at lower hydrothermal temperatures (80 and 130 °C), the corresponding XRD patterns were

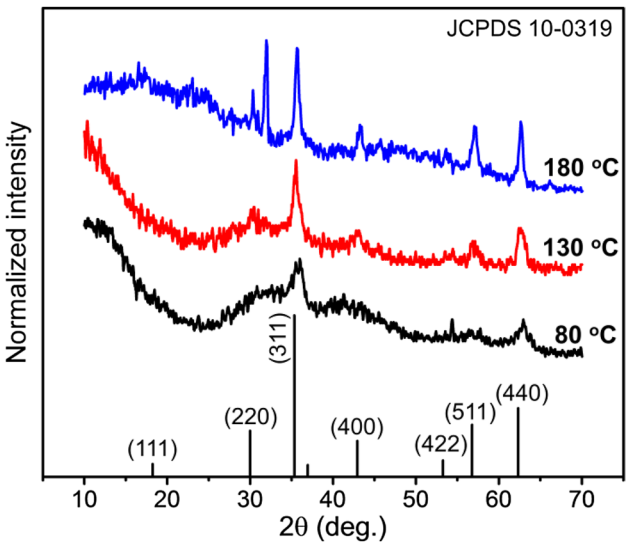

Fig. 2 XRD patterns of $rGO/MnFe_2O_4$ nanocomposites synthesized at different hydrothermal temperatures

all observed but with lower intensity and broader FWHM, indicating lower crystallinity and smaller crystallite size [26]. The occurrence of wide bands around (220) and (400) lattice planes indicate the possible presence of amorphous phases. The crystalline size of $MnFe_2O_4$ nanocrystals calculated from peak broadening using Scherrer's formula for (311) planes are 11.4, 17.9, and 37.2 nm, corresponding to $rGO/MnFe_2O_4$ nanocomposites prepared at 80, 130, and 180 °C. This suggests that increasing hydrothermal temperature leads to better crystallinity and higher crystalline size of $MnFe_2O_4$ nanoparticles on rGO sheets. The XRD analysis confirmed that $rGO/MnFe_2O_4$ nanocomposites have been successfully prepared at 80 and 130 °C.

The structure of $rGO/MnFe_2O_4$ nanocomposites was further studied by FTIR spectroscopy (Fig. 3a). In the FTIR spectrum of GO, a strong and broad band centered at 3304 cm^{-1} is attributed to the stretching vibration of –OH groups which are abundantly present in GO sheets and physically adsorbed water molecules. The peak at 1720 cm^{-1} belongs to carbonyl (C=O) stretching vibration. The peaks at 1628, 1408, 1178, and 1045 cm^{-1} are attributed to O–H bending, carboxy (C–O) stretching, C–OH stretching, and epoxy (C–O) stretching vibrations, respectively [10, 28, 29]. The peak at 874 cm^{-1} can be ascribed to =C–H out-of-plane vibrations. With the co-precipitation process and subsequent hydrothermal treatment, the peaks associated with the carbonyl (1720 cm^{-1}) and epoxy (1045 cm^{-1}) of $rGO/MnFe_2O_4$ nanocomposites almost disappeared, indicating the efficient reduction of GO (to rGO) and the possible presence of $MnFe_2O_4$ nanoparticles. Moreover, in the FTIR spectra of all composite samples, the bands corresponding to the –OH groups become weaker and shift to smaller

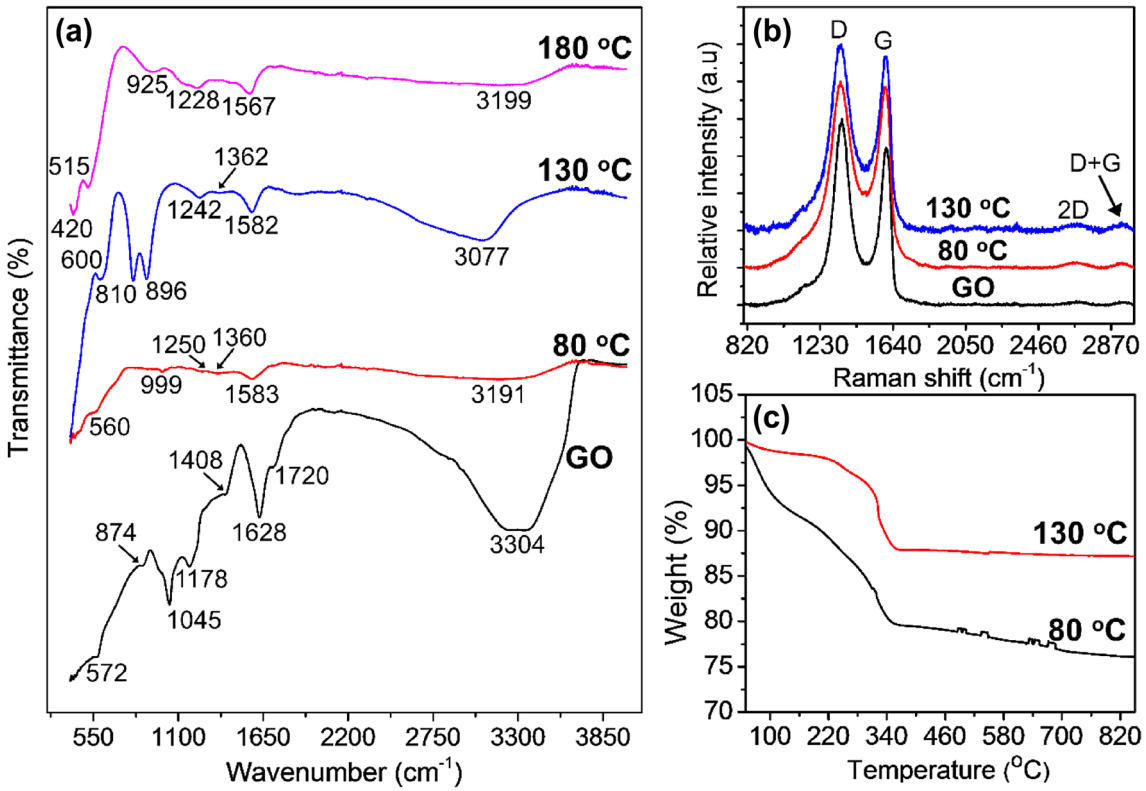

Fig. 3 **a** FT-IR spectra; **b** Raman spectra; and **c** thermogravimetric curves of GO sheets and rGO/$MnFe_2O_4$ nanocomposites synthesized at different hydrothermal temperatures

wavenumbers (3191, 3077, and 3199 cm^{-1}) as compared to that of GO (3304 cm^{-1}), suggesting a significant reduction in the amount of –OH groups. The new peaks at 1583, 1582, and 1567 cm^{-1} in nanocomposite samples can be attributed to vibrations of C=O in intercalated water. The peaks at 1250, 1242, and 1228 cm^{-1} in nanocomposite samples can be attributed to the presence of epoxide group. The stronger peaks at 896, 810, and 925 cm^{-1} might be originated from O–H and C–H groups, respectively. The peaks at 560, 600, 515 and 420 cm^{-1} are assigned to the vibrations of tetrahedral and octahedral sites in $MnFe_2O_4$ [8, 22]. These results confirmed the successful formation of rGO/$MnFe_2O_4$ nanocomposites.

Figure 3b shows Raman spectra of GO and rGO/$MnFe_2O_4$ nanocomposites prepared at 80 and 130 °C. All these spectra display two strong bands at ca. 1345 and 1598 cm^{-1}, which can be attributed to D and G bands of chemically-reduced GO, correspondingly [30]. The D band is due to the symmetry breaking of sp^2 carbon rings, derived from the oxidation of graphite during the Hummer's process [30] and reduction of GO (during hydrothermal treatment). The G band is caused by the E_{2g} vibrational mode of C-C bonds in sp^2 graphitic systems. In addition, these Raman spectra also exhibit second-order overtone (2D band) and combination Raman modes (D + G band), but with much weaker intensities. The calculated I_D/I_G ratios of rGO/$MnFe_2O_4$ nanocomposites prepared at 80 and 130 °C are all smaller than that of GO, indicating that GO has been also reduced during hydrothermal treatments.

Figure 3c shows TG curves of rGO/$MnFe_2O_4$ nanocomposites prepared at 80 and 130 °C. For the sample prepared at 130 °C, the first event of weight loss (up to ca. 220 °C) is attributed to the removal of adsorbed water. The second one (ca. 220–320 °C) is due to the decomposition of oxygen-containing functional groups remained in rGO. The third one (at ca. 320 nm) is obviously caused by the pyrolysis of carbon skeleton in rGO. The remaining weight of this sample is 87.16%, corresponding to the weight of $MnFe_2O_4$ phase. The sample prepared at 80 °C exhibited similar events, but the remaining weight of this sample is smaller (76.12%). Therefore, it is concluded that the higher the hydrothermal temperature, the better the reduction (of GO) and the higher the crystallinity of $MnFe_2O_4$.

3.1 Morphology and chemical composition of rGO/$MnFe_2O_4$ nanocomposites

Figure 4a represents SEM image of GO. It is obviously seen that GO sheets have been completely exfoliated from graphite, and their lateral sizes range from few to tens of

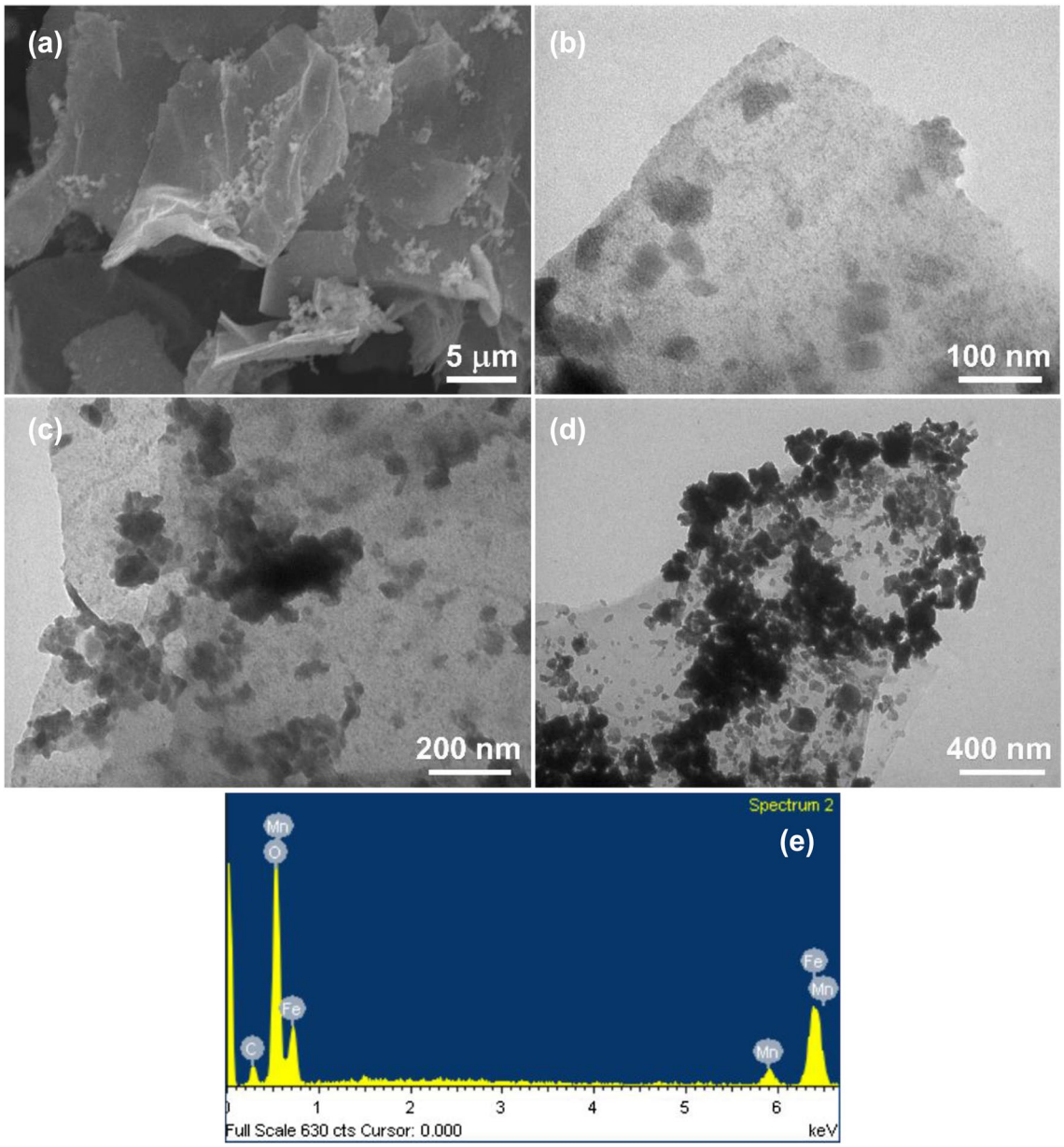

Fig. 4 **a** SEM image of GO. TEM images of rGO/$MnFe_2O_4$ nanocomposites synthesized at 80 °C (**b**), 130 °C (**c**), and 180 °C (**d**). **e** EDX spectrum of rGO/$MnFe_2O_4$ nanocomposites prepared at 80 °C

micrometers. Figure 4b–d represent TEM images of rGO/$MnFe_2O_4$ nanocomposites, which clearly show the growth and size development of $MnFe_2O_4$ nanocrystals on GO sheets. Upon increasing hydrothermal temperature, the size of $MnFe_2O_4$ nanocrystals increases and varies in the range of 5–40 nm. These values are slightly deviated from the crystalline size of $MnFe_2O_4$ nanocrystals estimated from XRD, which indicates $MnFe_2O_4$ nanocrystals are not uniformly monocrystalline. They are evenly distributed on rGO surface, suggesting rGO is a good substrate for the nucleation and growth of $MnFe_2O_4$ nanocrystals. The aggregation of bigger $MnFe_2O_4$ nanocrystals (Fig. 4c, d) can be attributed to a natural tendency of colloidal systems to decrease their surface energy and thus obtaining lower energy levels. In addition, magnetic interactions among $MnFe_2O_4$ nanocrystals could also promote the aggregation. Figure 4e represents a typical EDX spectrum of rGO/$MnFe_2O_4$ nanocomposites. The chemical composition of rGO/$MnFe_2O_4$ nanocomposites reflects the presence of all elements (C, O, Mn, Fe). For rGO/$MnFe_2O_4$ nanocomposites prepared at 80 °C, the average weight percentages of each element are 9.21% (C), 39.28% (O), 6.08% (Mn), and 45.43% (Fe). For rGO/

$MnFe_2O_4$ nanocomposites prepared at 130 °C, the average weight percentages of each element are 7.44% (C), 35.59% (O), 6.55% (Mn), and 50.43% (Fe). This indicates that rGO/$MnFe_2O_4$ nanocomposites have been successfully synthesized, and that the filtration and washing processes have efficiently removed excess precursors. It is thus proved that $MnFe_2O_4$ nanocrystals are occupied on the planar surface of rGO and suppresses the re-stacking of rGO sheets (through steric hindrance).

3.2 Magnetic properties

Magnetization curves of rGO/$MnFe_2O_4$ nanocomposites prepared at different hydrothermal temperatures are shown in Fig. 5. All nanocomposite samples exhibited superparamagnetic-like behavior, indicating small size of $MnFe_2O_4$ nanocrystals [18, 31]. Interestingly, their magnetic property is strongly correlated with hydrothermal temperature. Particularly, the saturated magnetization (M_s) of rGO/$MnFe_2O_4$ nanocomposites prepared at 80, 130, and 180 °C are 8.3, 15.4, and 22.7 emu/g, respectively. The M_s of the resulting nanocomposites is proportional to the temperature of hydrothermal treatment, indicating that increasing hydrothermal temperature leads to the improvement of magnetic properties. This property can be attributed to the fact that, upon increasing hydrothermal temperature, the crystallinity of $MnFe_2O_4$ nanocrystals is enhanced, as shown in XRD analysis. In addition, when the hydrothermal temperature increases, more GO sheets are reduced and thus the weight percentage of $MnFe_2O_4$ nanocrystals in the nanocomposites increases. As a result, the M_s of nanocomposites obtained at higher hydrothermal temperatures is improved. Higher M_s enables easy separation and recycle of the magnetic rGO/$MnFe_2O_4$ nanocomposites using external magnetic field, opening the possibility of using them in catalytic and environmental applications.

Graphene-based adsorbents have been widely studied for the removal of toxic pollutants including As(III) [32–35]. It was found that GO is better than rGO towards As(III) adsorption, and the As(III) adsorption mechanism is strongly related to surface complexation [33]. Previous studies showed that rGO/$MnFe_2O_4$ nanocomposites are efficient systems for As(III) adsorption because they possess various functional groups which are highly affinitive towards As(III). The mechanism and kinetics of the adsorption process have also been investigated [11, 20]. Herein, we performed the As(III) adsorption experiments on as-synthesized rGO/$MnFe_2O_4$ nanocomposites with the aim of evaluating their removal efficiency. The As(III) removal efficiency as a function of pH is shown in Fig. 6. It can be clearly seen that, at all pH values, the sample synthesized at higher temperature exhibits higher As(III) adsorption capacity. The rGO/$MnFe_2O_4$ nanocomposites synthesized at 180 °C exhibited highest As(III) removal efficiency of 83% at neutral pH (pH ≈ 7), which is nearly comparable with that of previous works [11, 20]. These results show that rGO/$MnFe_2O_4$ nanocomposites synthesized by combined hydrothermal/co-precipitation route could potentially be used as a magnetically recoverable adsorbents for environmental remediation.

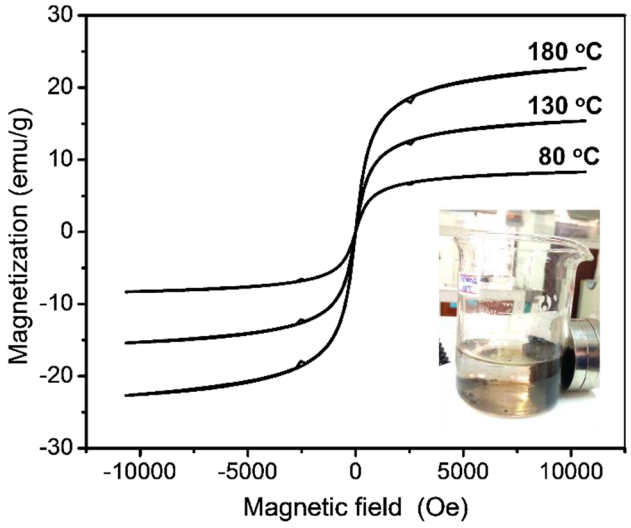

Fig. 5 Magnetization curves of rGO/$MnFe_2O_4$ nanocomposites prepared at different hydrothermal temperatures. Inset: An aqueous suspension of rGO/$MnFe_2O_4$ after placing near a permanent magnet

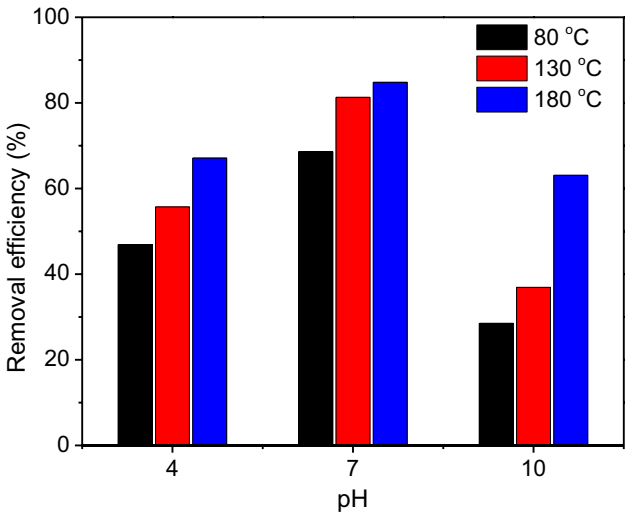

Fig. 6 Influence of pH on As(III) removal efficiency of rGO/$MnFe_2O_4$ nanocomposites synthesized at different hydrothermal temperatures

4 Conclusions

In summary, we successfully synthesized rGO/$MnFe_2O_4$ nanocomposites by a combined hydrothermal/co-precipitation route. $MnFe_2O_4$ nanocrystals were evenly grown on rGO sheets at high coverage. The results showed that when hydrothermal temperature increases from 80 to 180 °C, the size of $MnFe_2O_4$ crystallites increases from 11.4 to 37.2 nm, whereas M_s increases from 8.3 to 22.7 emu/g. Phase-pure rGO/$MnFe_2O_4$ nanocomposites were obtained at lower hydrothermal temperatures (80 and 130 °C). At higher hydrothermal temperature (180 °C), the presence of Fe_2O_3 phase was detected in rGO/$MnFe_2O_4$ nanocomposites. The nanocomposites synthesized at 180 °C exhibited highest performance towards As(III) adsorption. The current work provides a promising alternative for the synthesis of rGO/$MnFe_2O_4$ nanocomposites for environmental applications.

Acknowledgements This research is funded by Vietnam National Foundation for Science and Technology Development (NAFOSTED) under Grant number 103.02-2015.100.

References

1. Y. Wang, X. Wu, W. Zhang, S. Huang, One-pot synthesis of $MnFe_2O_4$ nanoparticles-decorated reduced graphene oxide for enhanced microwave absorption properties. Mater. Technol. **32**, 32–37 (2017)
2. I. Kotutha, E. Swatsitang, W. Meewassana, S. Maensiri, One-pot hydrothermal synthesis, characterization, and electrochemical properties of rGO/$MnFe_2O_4$ nanocomposites. Jpn. J. Appl. Phys. **54**, 06FH10 (2015)
3. S.-F. Zhou, X.-J. Han, H.-L. Fan, J. Huang, Y.-Q. Liu, Enhanced electrochemical performance for sensing Pb (II) based on graphene oxide incorporated mesoporous $MnFe_2O_4$ nanocomposites. J. Alloy. Compd. **747**, 447–454 (2018)
4. S. Chella, P. Kollu, E.V.P. Komarala, S. Doshi, M. Saranya, S. Felix, R. Ramachandran, P. Saravanan, V.L. Koneru, V. Venugopal, Solvothermal synthesis of $MnFe_2O_4$-graphene composite—investigation of its adsorption and antimicrobial properties. Appl. Surf. Sci. **327**, 27–36 (2015)
5. H. Tang, P. Gao, A. Xing, S. Tian, Z. Bao, One-pot low-temperature synthesis of a $MnFe_2O_4$–graphene composite for lithium ion battery applications. RSC Adv. **4**, 28421–28425 (2014)
6. K. Wu, G. Hu, Y. Cao, Z. Peng, K. Du, Facile and green synthesis of $MnFe_2O_4$/reduced graphene oxide nanocomposite as anode materials for Li-ion batteries. Mater. Lett. **161**, 178–180 (2015)
7. Z. Yang, Y. Huang, D. Ji, G. Xiong, H. Luo, Y. Wan, Hydrazine hydrate-induced hydrothermal synthesis of $MnFe_2O_4$ nanoparticles dispersed on graphene as high-performance anode material for lithium ion batteries. Ceram. Int. **43**, 10905–10912 (2017)
8. A.-T. Le, C.D. Giang, T.Q. Tuan, V.N. Phan, J. Alonso, J. Devkota, E. Garaio, J. García, R. Martín-Rodríguez, M.L. Fdez-Gubieda, Enhanced magnetic anisotropy and heating efficiency in multifunctional manganese ferrite/graphene oxide nanostructures. Nanotechnology **27**, 155707 (2016)
9. Y. Yang, H. Shi, Y. Wang, B. Shi, L. Guo, D. Wu, S. Yang, H. Wu, Graphene oxide/manganese ferrite nanohybrids for magnetic resonance imaging, photothermal therapy and drug delivery. J. Biomater. Appl. **30**, 810–822 (2016)
10. A.G. Tabrizi, N. Arsalani, A. Mohammadi, H. Namazi, L.S. Ghadimi, I. Ahadzadeh, Facile synthesis of a $MnFe_2O_4$/rGO nanocomposite for an ultra-stable symmetric supercapacitor. New J. Chem. **41**, 4974–4984 (2017)
11. S. Kumar, R.R. Nair, P.B. Pillai, S.N. Gupta, M. Iyengar, A. Sood, Graphene oxide–$MnFe_2O_4$ magnetic nanohybrids for efficient removal of lead and arsenic from water. ACS Appl. Mater. Interfaces **6**, 17426–17436 (2014)
12. S. Zhang, H. Niu, Y. Cai, X. Zhao, Y. Shi, Arsenite and arsenate adsorption on coprecipitated bimetal oxide magnetic nanomaterials: $MnFe_2O_4$ and $CoFe_2O_4$. Chem. Eng. J. **158**, 599–607 (2010)
13. S. Bai, X. Shen, X. Zhong, Y. Liu, G. Zhu, X. Xu, K. Chen, One-pot solvothermal preparation of magnetic reduced graphene oxide-ferrite hybrids for organic dye removal. Carbon **50**, 2337–2346 (2012)
14. X. Peng, J. Qu, S. Tian, Y. Ding, X. Hai, B. Jiang, M. Wu, J. Qiu, Green fabrication of magnetic recoverable graphene/$MnFe_2O_4$ hybrids for efficient decomposition of methylene blue and the Mn/Fe redox synergetic mechanism. RSC Adv. **6**, 104549–104555 (2016)
15. R. Rafiee, A. Eskandariyun, Comparative study on predicting Young's modulus of graphene sheets using nano-scale continuum mechanics approach. Phys. E **90**, 42–48 (2017)
16. N.U. Yamaguchi, R. Bergamasco, S. Hamoudi, Magnetic $MnFe_2O_4$–graphene hybrid composite for efficient removal of glyphosate from water. Chem. Eng. J. **295**, 391–402 (2016)
17. P.T.L. Huong, N. Tu, H. Lan, N. Van Quy, P.A. Tuan, N.X. Dinh, V.N. Phan, A.-T. Le, Functional manganese ferrite/graphene oxide nanocomposites: effects of graphene oxide on the adsorption mechanisms of organic MB dye and inorganic As (v) ions from aqueous solution. RSC Adv. **8**, 12376–12389 (2018)
18. C. Liu, Z.J. Zhang, Size-dependent superparamagnetic properties of Mn spinel ferrite nanoparticles synthesized from reverse micelles. Chem. Mater. **13**, 2092–2096 (2001)
19. R. Upadhyay, K. Davies, S. Wells, S. Charles, Preparation and characterization of ultra-fine $MnFe_2O_4$ and Mn_xFe_1–xFe_2O_4 spinel systems: I. particles. J. Magn. Magn. Mater **132**, 249–257 (1994)
20. P.T.L. Huong, V.N. Phan, T.Q. Huy, M.H. Nam, V.D. Lam, A.-T. Le, Application of graphene oxide-$MnFe_2O_4$ magnetic nanohybrids as magnetically separable adsorbent for highly efficient removal of arsenic from water. J. Electron. Mater. **45**, 2372–2380 (2016)
21. T.V. Thu, P.J. Ko, T.V. Nguyen, N.T. Vinh, D.M. Khai, L.T. Lu, Green synthesis of reduced graphene oxide/Fe_3O_4/Ag ternary nanohybrid and its application as magnetically recoverable catalyst in the reduction of 4-nitrophenol, Appl. Organomet. Chem. 31 (2017)
22. K.V. Sankar, R.K. Selvan, The preparation of $MnFe_2O_4$ decorated flexible graphene wrapped with PANI and its electrochemical performances for hybrid supercapacitors. RSC Adv. **4**, 17555–17566 (2014)
23. T.V. Thu, P.J. Ko, N.H.H. Phuc, A. Sandhu, Room-temperature synthesis and enhanced catalytic performance of silver-reduced graphene oxide nanohybrids. J. Nanoparticle Res. **15**, 1–13 (2013)
24. Y. Sang, H. Liu, X. Sun, X. Zhang, H. Qin, Y. Lv, D. Huo, D. Liu, J. Wang, R.I. Boughton, Formation and calcination temperature-dependent sintering activity of YAG precursor synthesized via reverse titration method. J. Alloy. Compd. **509**, 2407–2413 (2011)
25. Y. Sang, Y. Lv, H. Qin, X. Zhang, H. Liu, J. Wang, X. Sun, R.I. Boughton, Chemical composition evolution of YAG co-precipitate determined by pH during aging period and its effect on precursor properties. Ceram. Int. **38**, 1635–1641 (2012)
26. A. Patterson, The Scherrer formula for X-ray particle size determination. Phys. Rev. **56**, 978 (1939)

27. H. Cui, Y. Liu, W. Ren, Structure switch between α-Fe_2O_3, γ-Fe_2O_3 and Fe_3O_4 during the large scale and low temperature sol–gel synthesis of nearly monodispersed iron oxide nanoparticles. Adv. Powder Technol. **24**, 93–97 (2013)
28. Y. Jiang, C. Hu, H. Cheng, C. Li, T. Xu, Y. Zhao, H. Shao, L. Qu, Spontaneous, straightforward fabrication of partially reduced graphene oxide–polypyrrole composite films for versatile actuators. ACS Nano **10**, 4735–4741 (2016)
29. G. Titelman, V. Gelman, S. Bron, R. Khalfin, Y. Cohen, H. Bianco-Peled, Characteristics and microstructure of aqueous colloidal dispersions of graphite oxide. Carbon **43**, 641–649 (2005)
30. K.N. Kudin, B. Ozbas, H.C. Schniepp, R.K. Prud'Homme, I.A. Aksay, R. Car, Raman spectra of graphite oxide and functionalized graphene sheets. Nano Lett. **8**, 36–41 (2008)
31. C. Liu, B. Zou, A.J. Rondinone, Z.J. Zhang, Reverse micelle synthesis and characterization of superparamagnetic $MnFe_2O_4$ spinel ferrite nanocrystallites. J. Phys. Chem. B **104**, 1141–1145 (2000)
32. V. Chandra, J. Park, Y. Chun, J.W. Lee, I.-C. Hwang, K.S. Kim, Water-dispersible magnetite-reduced graphene oxide composites for arsenic removal. ACS Nano **4**, 3979–3986 (2010)
33. Y. Yoon, W.K. Park, T.-M. Hwang, D.H. Yoon, W.S. Yang, J.-W. Kang, Comparative evaluation of magnetite–graphene oxide and magnetite-reduced graphene oxide composite for As (III) and As (V) removal. J. Hazard. Mater. **304**, 196–204 (2016)
34. G. Zhao, J. Li, X. Ren, C. Chen, X. Wang, Few-layered graphene oxide nanosheets as superior sorbents for heavy metal ion pollution management. Environ. Sci. Technol. **45**, 10454–10462 (2011)
35. X. Luo, C. Wang, L. Wang, F. Deng, S. Luo, X. Tu, C. Au, Nanocomposites of graphene oxide-hydrated zirconium oxide for simultaneous removal of As (III) and As (V) from water. Chem. Eng. J. **220**, 98–106 (2013)